

# Reconciling Semiclassical and Bohmian Mechanics: IV. Multisurface Dynamics

Bill Poirier

*Department of Chemistry and Biochemistry, and Department of Physics,  
Texas Tech University, Box 41061, Lubbock, Texas 79409-1061\**

G erard Parlant

*Institut Charles Gerhardt, Universit  Montpellier 2, CNRS,  
Equipe CTMM, case courrier 1501, place Eug ne bataillon, 34095 Montpellier, France†*

In previous articles [J. Chem. Phys. **121** 4501 (2004), J. Chem. Phys. **124** 034115 (2006), J. Chem. Phys. **124** 034116 (2006)] a bipolar counter-propagating wave decomposition,  $\Psi = \Psi_+ + \Psi_-$ , was presented for stationary states  $\Psi$  of the one-dimensional Schr dinger equation, such that the components  $\Psi_{\pm}$  approach their semiclassical WKB analogs in the large action limit. The corresponding bipolar quantum trajectories are classical-like and well-behaved, even when  $\Psi$  has many nodes, or is wildly oscillatory. In this paper, the method is generalized for multisurface scattering applications, and applied to several benchmark problems. A natural connection is established between intersurface transitions and  $(+ \leftrightarrow -)$  transitions.

## I. INTRODUCTION

This paper is the fourth in a series<sup>1,2,3</sup> investigating the use of “counter-propagating wave methods” (CPWMs)<sup>1,2,3,4,5,6</sup> for solving the time-independent Schr dinger equation exactly. The basic idea is to decompose the stationary wavefunction,  $\Psi$ , into a two-term, or “bipolar” form,

$$\Psi = \Psi_+ + \Psi_-, \quad (1)$$

such that the  $\Psi_+$  and  $\Psi_-$  represent wave “components” moving in opposite directions. Although Eq. (1) is exact, the particular bipolar decomposition used is chosen to correspond to analogous approximate semiclassical wave components.<sup>7,8,9</sup> For smooth potentials, the latter are known to exhibit smooth and slowly-varying field functions throughout the interaction region. The exact  $\Psi_{\pm}$  of Eq. (1) must behave similarly, at least in the classical limit, and in any case lead to field functions that are much better behaved than for  $\Psi$  itself. For stationary scattering states, for instance,  $\Psi$  necessarily exhibits oscillatory interference in one or more asymptotic regions where the interaction potential  $V$  is flat, whereas the asymptotic  $\Psi_+$  and  $\Psi_-$  behave as plane waves. Thus, interference manifests not in the individual components, but arises naturally from their linear superposition.

Apart from certain conceptual and theoretical advantages, the above picture is particularly relevant for quantum trajectory methods (QTMs)<sup>6,10,11,12,13,14,15,16,17,18,19,20</sup>—i.e., trajectory-based numerical techniques for performing exact quantum dynamics calculations, in a manner similar to classical simulations.<sup>21</sup> QTMs that are based on standard Bohmian mechanics<sup>22,23,24,25,26,27</sup> use a single-term or “unipolar” representation of the wavefunction, from which the quantum trajectory evolution is determined. However, the Bohmian time evolution equations are nonlinear, which can lead to radically different QTM

behavior when applied to the individual bipolar components of Eq. (1), rather than to  $\Psi$  itself. In particular, the smooth field functions of the  $\Psi_{\pm}$  obviate the “node problem”—i.e. the near-singularities in the quantum potential,  $Q$ , leading to numerical instabilities in the quantum trajectory evolution when there is substantial interference.<sup>5,6,15,28,29,30</sup> A more detailed discussion may be found in the previous articles cited above.

For one-dimensional (1D) stationary scattering state calculations, the bipolar CPWM trajectories are actually *classical*, in a certain generalized sense (Sec. II and Ref. 4). Quantum effects arise not from a quantum potential,  $Q$ , impacting trajectory evolution, but rather through dynamical coupling between the two components,  $\Psi_+$  and  $\Psi_-$ . This coupling, which is in essence proportional to the interaction potential, induces  $(+ \leftrightarrow -)$  transitions—i.e., scattering from the  $\Psi_+$  incident/transmitted wave to the  $\Psi_-$  reflected wave, and vice-versa. In many respects, the situation is reminiscent of traditional multisurface scattering theory, in which an off-diagonal diabatic coupling potential induces a dynamical transition from one diabatic state to another. Indeed, one somewhat compelling conclusion of the present work—which deals with a bipolar CPWM treatment of multisurface dynamics—is that in some sense *both types of transitions may be regarded as different aspects of the same underlying phenomenon*. This “unification” may result in an interesting cross-fertilization of ideas, e.g. in the area of classical trajectory surface hopping (TSH) methodologies, originally designed by Tully.<sup>31,32</sup>

We are by no means the first to apply QTMs to the dynamics of electronic nonadiabatic collisions; the first papers to do so were written several years ago by Wyatt and coworkers.<sup>14,17</sup> It should be noted that Wyatt’s treatment is exact—at least formally—although approximate and/or classical versions have also been developed.<sup>33,34,35</sup> These methods are often compared to TSH, with which they (and the present approach) have important differ-

ences. In TSH, a swarm of independent classical trajectories evolve along a given potential energy surface; for each trajectory, a decision is made whether to “hop” to a different surface, based upon a transition probability, obtained by integrating coupled equations for the electronic amplitudes. In contrast, the above multisurface methods do not involve any trajectory hopping (the number of trajectories evolving on each electronic surface is, in fact, conserved) but transfer density and phase information from one state to another in a continuous manner. Note that—like its single surface counterpart—the multisurface QTM of Wyatt et al. is based on a unipolar representation of the wavefunction, and is therefore also subject to numerical instabilities due to interferences. Moreover, in the multisurface case, interference arises not only from waves propagating in opposite directions on the same surface, but also from waves transferring flux from one surface to another.

It should also be stated that in the multisurface context, the idea of applying a bipolar decomposition has been previously considered. In particular, M. Alexander and coworkers adopted such a scheme in the exact quantum solution of the close-coupling equations using log-derivative propagation,<sup>36,37</sup> although their choice of Eq. (1) decomposition does not avoid oscillatory field functions, and is therefore not so useful for QTMs. D. V. Shalashilin also used a bipolar decomposition to solve the close-coupling equations (for inelastic scattering applications), albeit only as a semiclassical approximation.<sup>38,39</sup>

The remainder of this paper is organized as follows. Sec. II discusses theoretical and algorithmic developments, both for single surface dynamics calculations (Sec. IIA) and the multisurface case (Secs. IIB and IIC). Note that the bipolar CPWM algorithms used here require neither complex scaling<sup>40,41,42</sup> nor absorbing potentials<sup>43,44,45,46</sup>—a decided advantage over other quantum scattering methods. Moreover, the scaling of computational (CPU) effort is linear with the grid size,  $N$ , rather than proportional to  $N^3$ . Results are presented in Sec. III. For single surface applications (Sec. IIIA), in addition to a test suite of wide-ranging applications considered previously,<sup>4</sup> we investigate the ability of the method to compute scattering quantities to extremely high relative accuracy, or precision. Several benchmark two-surface applications are considered in Sec. IIIB, including two of the Tully models.<sup>32</sup> Concluding remarks are given in Sec. IV.

## II. THEORY AND ALGORITHM DEVELOPMENT

### A. Single Surface Dynamics

In several previous articles,<sup>2,3,4</sup> an extremely accurate, efficient, and robust bipolar CPWM numerical algorithm was developed for computing stationary scattering states of 1D single-surface systems. A brief summary is pre-

sented here; further details can be found in the above-referenced articles.

The algorithm is a time-dependent relaxation method, for which the initial wavefunction is a left-incident/transmitted wave only, i.e.  $\Psi(x, t = 0) = \Psi_+(x, t = 0)$  and  $\Psi_-(x, t = 0) = 0$ . Over time, a reflected wave  $\Psi_-(x, t)$  comes into being through interaction region coupling due to the potential energy, and eventually  $\Psi(x, t) = \Psi_+(x, t) + \Psi_-(x, t)$  relaxes to the true stationary eigenstate of desired energy,  $E$ , and left-incident boundary conditions. The solution components  $\Psi_{\pm}(x)$  behave as (right/left) traveling plane waves in both asymptotes, except that  $\lim_{x \rightarrow \infty} \Psi_-(x) = 0$ . The asymptotic square amplitudes,  $\lim_{x \rightarrow \infty} |\Psi_+(x)|^2$  and  $\lim_{x \rightarrow -\infty} |\Psi_-(x)|^2$ , are directly related to transmission and reflection probabilities, respectively [Eq. (14)]. Through the interaction region, the solution  $\Psi_{\pm}(x)$ ’s are exact quantum analogues of a type of semiclassical WKB approximation resulting from the “generalized Fröman” (F) approach.<sup>3,4,8</sup> Amplitude and phase functions for the  $\Psi_{\pm}$  components are expected to be smooth and slowly varying, unlike those for the solution  $\Psi$  itself.

The “generalized” aspect of the above methodology implies that we are formally allowed to specify the “classical” trajectories as we wish, using an effective potential  $V^{\text{eff}}(x)$  of our own choosing, rather than the actual potential  $V(x)$ . In practice, the method requires that  $\lim_{x \rightarrow \pm\infty} [V(x) - V^{\text{eff}}(x)] = 0$ , and works best when  $V^{\text{eff}}(x)$  is smooth and monotonic between the two asymptotes. This ensures that all trajectories are devoid of turning points, and that there is no asymptotic coupling between the two  $\Psi_{\pm}$  components. Note that the  $\Psi_+(x)$  trajectories move to the right with velocity  $v(x) = \sqrt{2[E - V^{\text{eff}}(x)]/m}$ , and the  $\Psi_-(x)$  trajectories move to the left with equal and opposite velocity  $-v(x)$ . As per other QTM’s, the trajectories give rise to discrete moving grids, which carry local phase and amplitude information for the appropriate  $\Psi_{\pm}$  component. There is no quantum potential<sup>6,27</sup> contributing to the dynamics; all trajectories are (generalized) classical, and can be determined *a priori*. Instead, quantum effects manifest via  $\Psi_{\pm}$  coupling in the interaction region—as evidenced by the time evolution equations (Ref. 4 Eq. (16), or Eq. (7) of this article with  $f = 1$ ). The coupling is essentially proportional to the interaction potential, and can be said to induce transitions from one  $\Psi_{\pm}$  component to the other.

In the previous papers, various numerical innovations were introduced to improve performance and stability of the trajectory-based time propagation of  $\Psi_{\pm}$ , designed to deal effectively with the unusual mixed boundary conditions [Eq. (13)]. First, since the upper (+) and lower (−) grids are moving in opposite directions, they cannot be commensurate at all times. However, a scheme was introduced whereby these two grids are commensurate at all times  $t$  equal to a multiple of the “shift time,”  $t_{\text{shift}}$ —the time it takes one grid point to travel to the lo-

cation vacated by its nearest neighbor. A constraint on  $t_{\text{shift}}$  is that it be a multiple of the propagation time step size,  $\Delta$ . Second, since grids are generally incommensurate, interpolation must be used to evaluate the coupling contribution—a procedure found to yield far better results when applied to a *polar* (amplitude/phase) decomposition of the  $\Psi_{\pm}$ 's, rather than directly to the  $\Psi_{\pm}$ 's themselves. A “plane wave propagator” (PWP) approach was also employed, which effectively treats the uncoupled part of the time evolution equations exactly, and the coupled part using first-order Euler time integration.

Unfortunately, the PWP idea is found to be generally incompatible with more efficient time integrators, such as fourth-order Runge-Kutta (adaptive and non-adaptive), used here. Note that for symmetric potential systems, it is possible to recast the time evolution equations in such a way that the PWP contribution vanishes (by introducing a time-evolving phase into the definition of the wavefunction). In order to ascertain the extent to which PWP actually improves performance, some preliminary numerical tests were conducted for the Eckart A system (Sec. III) with  $E = V_0$ . In particular, an efficiency comparison was made between the original PWP algorithm and the “phase-modified” version—both using first-order Euler propagation for the non-PWP contribution. For an identical set of numerical parameters, both methods performed about equally well, vis-à-vis the accuracy of the computed reflection and transmission probabilities—although the phase-modified version executed roughly 30% faster, owing to less required computation. As a second, more realistic test, the phase-modified algorithm with fourth-order Runge-Kutta was compared to a straight fourth-order Runge-Kutta treatment of all terms in the original evolution equations (including PWP terms). Both methods again performed roughly equally well with respect to computed accuracy, with slight performance differences depending on the desired level of accuracy. Moreover, both methods are far superior to the first-order Euler methods, enabling  $\Delta$  values that are orders of magnitude larger, without compromising numerical accuracy. Only the straight Runge-Kutta method can be generalized for asymmetric potential systems, however, and is introduced here as the general method of choice.

We also introduce an improved method for dealing with extremal trajectories that stray outside the range of interpolation: instead of ignoring the coupling contribution altogether,<sup>4</sup> we now simply use values for the polar field quantities obtained from the nearest extremal grid point—although it should be emphasized that the true coupling contribution is vanishingly small in the asymptotic limit. Also, even within the range of interpolation, the interpolated density value may become slightly negative when the density absolute values are very small; in that case, we now reset the interpolated value to zero.

## B. Multisurface Dynamics: Theory

We now generalize the theory for the 1D multisurface case. Note that only a brief summary is provided here, as the full derivation follows closely that of Refs. 3 and 4, which should be consulted for further details.

Let  $f$  be the number of electronic states considered, with no restrictions on intersurface coupling. A diabatic-like time-independent matrix Schrödinger equation is presumed, of the form

$$\tilde{H} \cdot \vec{\Psi} = E\vec{\Psi}, \quad (2)$$

where  $\{\Psi_1, \Psi_2, \dots, \Psi_f\}$  comprise the vector components (associated with each of the  $f$  diabatic states) of the nuclear wavefunction,  $\vec{\Psi}$ , and

$$[\tilde{H}]_{i,j} = -\delta_{i,j} \left( \frac{\hbar^2}{2m} \right) \frac{\partial^2}{\partial x^2} + V_{i,j}(x) \quad (3)$$

are the components of the  $f \times f$  Hamiltonian operator matrix,  $\tilde{H}$ , with  $i \leq f$  and  $j \leq f$  labeling diabatic states.

The  $V_{i,j}(x) = V_{j,i}(x)$  are the diabatic potential energy curves, with the  $i \neq j$  case denoting the coupling potentials. In order to ensure that coupling vanishes in the asymptotic limits (required to obtain asymptotic scattering waves with correct boundary conditions),<sup>3,4</sup> we must have  $\lim_{x \rightarrow \pm\infty} V_{i \neq j}(x) = 0$ . However, the asymptotic values for the diagonal potentials,  $V_{i,i}(x)$ , are allowed to be completely arbitrary, and in particular, need not be symmetric. Left and right asymptotic values are denoted  $V_{iL} = \lim_{x \rightarrow -\infty} V_{i,i}(x)$  and  $V_{iR} = \lim_{x \rightarrow \infty} V_{i,i}(x)$ , respectively. For purposes of generating trajectories for motion on the  $i$ 'th diabatic state, a suitable family of  $f$  effective potentials,  $V_i^{\text{eff}}(x)$ , are introduced, such that  $\lim_{x \rightarrow \pm\infty} [V_{i,i}(x) - V_i^{\text{eff}}(x)] = 0$  (to ensure against asymptotic coupling), and  $V_i^{\text{eff}}(x) \leq \max(V_{iR}, V_{iL})$  for all  $x$  (to avoid turning points, as discussed in Sec. II A).

Assuming that each component of  $\vec{\Psi}$  is decomposed into its own bipolar expansion,

$$\Psi_i(x) = \Psi_{i+}(x) + \Psi_{i-}(x), \quad (4)$$

we clearly need  $2f$  independent differential equations [and associated boundary conditions (Sec. II C)], to uniquely specify the solution decomposition of Eq. (4). One half of these are already provided in Eqs. (2) and (3). For the remaining  $f$  equations, it is natural to apply the generalized  $F$  approach (Sec. II A) in component-wise fashion. In particular, for a single-surface system, the generalized  $F$  approach<sup>8</sup> provides the following as the second (after the usual Schrödinger equation) independent differential condition,

$$\Psi' = -\frac{v'}{2v}\Psi + \frac{imv}{\hbar}(\Psi_+ - \Psi_-) \quad (5)$$

(where the prime denotes spatial differentiation), as discussed in more detail in Ref. 4 [Eq. (11)]. For the multisurface generalization, we simply apply Eq. (5) to each

adiabatic state separately, to obtain

$$\Psi_i' = -\frac{v_i'}{2v_i} \Psi_i + \frac{imv_i}{\hbar} (\Psi_{i+} - \Psi_{i-}), \quad (6)$$

where  $v_i(x) = \sqrt{2[E - V_i^{\text{eff}}(x)]/m}$  are the trajectory velocities for the  $i$ 'th diabatic state (as determined by the effective potential  $V_i^{\text{eff}}$ ). Note that Eq. (6) does not depend at all on the  $V_{i \neq j}$  as appropriate, i.e. all intersurface coupling should arise through the Schrödinger Eq. (2), itself, if  $(+ \leftrightarrow -)$  transitions for single- and multi-surface applications are to be treated equally.

By combining Eq. (2) with Eq. (6), we can derive expressions for the first spatial derivatives of each of the  $2f$  bipolar CPWM components, i.e. the  $\Psi_{i\pm}'$ , directly in terms of the undifferentiated component quantities. This yields somewhat complicated results, analogous to Ref. 4 Eq. (12), which are excluded here for the sake of brevity. By following the procedure described in detail in Ref. 3 and Ref. 4 [basically, constructing a convective term to get rid of first-order spatial derivatives of the wavefunction in the hydrodynamic frame, and introducing an explicit time dependence via  $\partial\Psi_{\pm}/\partial t = -(i/\hbar)E\Psi_{\pm}$ ], we are then led to the following coupled hydrodynamic (Lagrangian) time evolution equations:

$$\begin{aligned} \frac{d\Psi_{i\pm}}{dt} = & \left[ \pm \frac{1}{4} v_i \left( \frac{V_i^{\text{eff}'}}{E - V_i^{\text{eff}}} \right) + \frac{i}{\hbar} (E - V_{i,i} - V_i^{\text{eff}} + C_i) \right] \Psi_{i\pm} \\ & - \frac{i}{\hbar} [V_{i,i} - V_i^{\text{eff}} - C_i] \Psi_{i\mp} - \frac{i}{\hbar} \sum_{j \neq i}^f V_{i,j} (\Psi_{j+} + \Psi_{j-}), \end{aligned} \quad (7)$$

where,

$$C_i = \left( \frac{\hbar^2}{2m} \right) \left[ \frac{5}{16} \left( \frac{V_i^{\text{eff}'}}{E - V_i^{\text{eff}}} \right)^2 + \frac{1}{4} \left( \frac{V_i^{\text{eff}''}}{E - V_i^{\text{eff}}} \right) \right] \quad (8)$$

For pedagogical purposes, we also consider the asymptotically symmetric special case with  $V_{iL} = V_{iR} = 0$  and  $V_i^{\text{eff}}(x) = 0$  for all  $i$ :

$$\frac{d\Psi_{i\pm}}{dt} = \frac{i}{\hbar} \left[ E\Psi_{i\pm} - \sum_{j=1}^f V_{i,j} (\Psi_{j+} + \Psi_{j-}) \right] \quad (9)$$

Note: in Eq. (9),  $j$  ranges over all values, including  $j = i$ .

The time evolution equations of the preceding paragraph—best exemplified by Eq. (9)—offer a coherent, unified picture of scattering theory that places both intersurface transitions and  $(+ \leftrightarrow -)$  transitions on a near-equal footing. Note first that coupling of all types vanishes in both asymptotic limits, resulting in uncoupled, scattering plane wave dynamics in these limits for all  $\Psi_{i\pm}$ , as desired. In particular,  $\Psi_{i\pm}(x \rightarrow \pm\infty, t)$  is

a plane wave propagating to the (right/left) with uniform speed  $v_{iL/R} = \sqrt{2[E - V_{iL/R}]/m}$ . It is the various potential interactions, operating in the interaction region, that induce transitions of all kinds among the  $2f$  bipolar CPWM components,  $\Psi_{i\pm}$ . The off-diagonal potentials  $V_{i \neq j}$  are responsible for transitions between diabatic states  $i$  and  $j$ , whereas the diagonal potentials  $V_{i,i}$  induce transitions from reactive (transmitted)  $\Psi_{i+}$  to non-reactive (reflected)  $\Psi_{i-}$  components (and vice-versa). Apart from this distinction, both types of transitions manifest similarly in the equations of motion.

As in the previous work,<sup>3,4</sup> the time evolution equations above give rise to some elegant flux properties, which again treat both types of transitions (or probability flow) on a near-equal footing. Let  $j_{i\pm} = \pm v_i \rho_{i\pm}$  be the flux for component  $\Psi_{i\pm}$ , defined in terms of the generalized trajectory velocities  $v_i$ , and the component probability densities,  $\rho_{i\pm} = |\Psi_{i\pm}|^2$ . We also find it convenient to introduce new composite labels,  $\alpha = (i, \pm)$  and  $\beta = (j, \pm)$ , to label individual  $\Psi_{i\pm}$  components. Note that the  $\pm$  values are *independent* for  $\alpha$  and  $\beta$ , so that each of these two component labels can take on  $2f$  distinct values. Using Eq. (7), and transforming to Eulerian (partial) time derivatives, we obtain the following flux relation:

$$\frac{\partial \rho_{\alpha}}{\partial t} = -j_{\alpha}' + \sum_{\beta \neq \alpha} \frac{\partial \rho_{\text{cpl}}^{\alpha \leftarrow \beta}}{\partial t}, \quad (10)$$

where

$$\frac{\partial \rho_{\text{cpl}}^{\alpha \leftarrow \beta}}{\partial t} = \frac{2}{\hbar} [V_{i,j} - \delta_{i,j} (V_i^{\text{eff}} + C_i)] \text{Im} [\Psi_{\alpha}^* \Psi_{\beta}], \quad (11)$$

and  $\partial \rho_{\text{cpl}}^{\alpha \leftarrow \beta} / \partial t$  represents the rate of probability density flow from component  $\beta$  to  $\alpha$ .

Equations (10) and (11) above emphasize the essential similarities between the two types of transitions—particularly for the  $V_{iL} = V_{iR} = 0$  case, for which the  $\delta_{i,j}$  contribution in Eq. (11) vanishes. More importantly, however, we find that  $\partial \rho_{\text{cpl}}^{\alpha \leftarrow \beta} / \partial t = -\partial \rho_{\text{cpl}}^{\beta \leftarrow \alpha} / \partial t$ , which implies the nontrivial combined continuity relation,<sup>3,4</sup>

$$\frac{\partial \sum_{\alpha} \rho_{\alpha}}{\partial t} = - \sum_{\alpha} j_{\alpha}'. \quad (12)$$

Equation (12) further implies that the total probability integrated over all  $2f$  components is conserved over time—a desirable but nontrivial result, given that  $\Psi_{i+}$  and  $\Psi_{i-}$  are not true “components” (orthogonal complements) in the way that  $\Psi_i$  and  $\Psi_{j \neq i}$  are.

The above discussion regarding time evolution properties pertains to all times,  $t$ —not just the  $t \rightarrow \infty$  limit, where  $\bar{\Psi}$  approaches the exact stationary solution. In the latter limit, however, it is clear that Eq. (12) must be zero, so that the stationary solution must satisfy  $j_{+}' = -j_{-}'$ , where  $j_{\pm} = \sum_{i=1}^f j_{i\pm}$  represents the total flux moving in the (right/left) directions. For the

$V_{iL} = V_{iR} = 0$  case in particular, this implies that  $\rho_{+'} = \rho_{-}'$ , where  $\rho_{\pm} = \sum_{i=1}^f \rho_{i\pm}$ . In other words, the sum of all + densities is equal to the sum of all - densities, apart from a constant—a nice generalization of Ref. 3 Eq. (15).

### C. Multisurface Dynamics: Numerical Algorithm

To implement the above time evolution equations numerically, we must first discuss boundary conditions and initial value conditions. Without loss of generality, we may assume an incoming wave that is left-incident on the diabatic state  $i = 1$ . Probability flow from  $\Psi_{1+}$  to the other CPWM components occurs only in the interaction region, and then propagates outward towards the appropriate asymptotes. Adopting the usual normalization convention thus leads to the following boundary conditions:

$$\begin{aligned} \Psi_{1+}(x \rightarrow -\infty) &= \exp \left[ +i \left( \frac{\sqrt{2m(E - V_{1L})} x}{\hbar} - \phi \right) \right] \\ \Psi_{(i>1)+}(x \rightarrow -\infty) &= 0 \\ \Psi_{i-}(x \rightarrow \infty) &= 0 \end{aligned} \quad (13)$$

In Eq. (13) above,  $\phi$  is a time-dependent phase factor.

As for the initial value, we take  $\Psi_{\alpha}(x, t = 0) = 0$  for all  $\alpha$  except  $\alpha = (1, +)$ , for which the basic WKB solution is used, as described in Ref. 4 Eq. (18). In the  $t \rightarrow \infty$  limit, the resultant numerical solution  $\Psi_{i\pm}$ 's can be directly consulted to obtain transmission probabilities [associated with  $\rho_{i+}(x \rightarrow \infty)$ ] and reflection probabilities [associated with  $\rho_{i-}(x \rightarrow -\infty)$ ], as per Eq. (14).

In most respects, the numerical algorithm employed for the time evolution is identical to that discussed in Sec. II A. One complicating factor is that the trajectories [determined from  $v_i(x)$ ] are obviously completely different from one diabatic state,  $i$ , to the next. In a single-surface calculation, the + and - grid points move in opposite directions. Thus, the two grids must be incommensurate for most times, although a simple scheme is used to ensure commensurate grids when  $t$  is a multiple of the shift time,  $t_{\text{shift}}$ . Starting at the left edge of the grid,  $x_L$ , one propagates a *single* trajectory,  $x(t)$ . The initial grid for both + and - is then taken to be the values  $x_k = x(t = kt_{\text{shift}})$  for nonnegative integers,  $k$  such that  $x_k < x_R$ , where  $x_R$  is the right edge of the grid.<sup>4</sup>

In the multisurface case, the trajectories at a given point  $x$  move with different speeds for different  $i$  values, thus rendering it impossible for grids to be commensurate across diabatic states, even at regular time intervals. A reasonable procedure, however, is to apply the above in component-wise fashion, i.e. by generating a family of  $f$  trajectories,  $x_i(t)$ . If the same  $t_{\text{shift}}$  value is used for all  $i$ , then at intervals  $t = kt_{\text{shift}}$ , the  $i+$  and  $i-$  grids will be commensurate with each other, for all  $i$  (but still not *across*  $i$  values). The nonuniform grids generated in this fashion will be denser where  $v_i$  is smaller—which

is physically reasonable, and in any event is also true in the single-surface case. To evaluate the intersurface coupling contribution in Eq. (7), a polar intersurface grid interpolation scheme is used, exactly analogous to that used for  $(+ \leftrightarrow -)$  coupling in the single-surface case. Note that all grids extend over the full coordinate range, i.e. roughly from  $x_L$  to  $x_R$ .

## III. RESULTS

In this section, we discuss the application of the numerical algorithms described in Sec. II to a variety of model systems. The mass  $m = 2000$  a.u. was used in all cases. Also, fourth-order Runge-Kutta time integrators were employed, as was natural spline interpolation, unless stated otherwise. For the symmetric, single-surface potentials, the phase-modified algorithm was used. A thorough and detailed convergence study was performed for each system, by varying each of the convergence parameters in turn, and monitoring associated changes to the computed reflection and transmission probabilities,  $P_i^{\text{refl}}$  and  $P_i^{\text{trans}}$ . Unless stated otherwise, the precise convergence procedure followed is that described in Ref. 4, with one exception: since “oscillatory error” was always found to be negligible, reflection and transmission probabilities are defined here to be

$$\begin{aligned} P_i^{\text{refl}} &= (v_{iL}/v_{1L}) |\Psi_{i-}(x_L)|^2 \\ P_i^{\text{trans}} &= (v_{iR}/v_{1L}) |\Psi_{i+}(x_R)|^2, \end{aligned} \quad (14)$$

where  $v_{iL/R} = \lim_{x \rightarrow \mp \infty} v_i(x)$ ,

rather than as described in Ref. 4.

### A. Single Surface Applications

As fourth-order Runge-Kutta integrators have not been previously combined with the numerical innovations of Ref. 4 (Sec. II A), our first task is to evaluate the numerical efficacy of the present approach for single surface systems. In particular, we apply the method to a “test suite” of 1D benchmark applications<sup>3,4</sup> exhibiting a range of different attributes with regard to tunneling, barrier height and width, exoergicity, existence of reaction intermediates, and desired level of computational accuracy. In doing so, the robustness and stability of the method will be evaluated, as well as the numerical efficiency, as compared with the previous codes.

Only a brief description of the individual test suite applications will be provided here; for additional details, the previous papers may be consulted. The five test suite potentials are as follows:

- **Eckart A:** short, narrow Eckart barrier (height  $V_0 \approx 0.0018$  hartree)
- **Eckart B:** tall, wide Eckart barrier (height  $V_0 = 0.011$  hartree)

- **Uphill ramp:** tanh potential, barrierless and monotonic ( $V_R - V_L \approx 0.0018$  hartree)
- **Barrier ramp:** Eckart + tanh potential, asymmetric with barrier ( $V_R - V_L \approx 0.0018$  hartree)
- **Double barrier:** symmetric double barrier with reaction intermediate well (barrier height  $V_0 \approx 0.0018$  hartree)

Results are presented in Table I.

In the first investigation, we computed  $P^{\text{refl}}$  and  $P^{\text{trans}}$  for each of the five test suite potentials above, at an energy  $E \approx V_0$  or  $E \approx (V_R - V_L)$  (Table I, Row 1) chosen to yield both substantial reflection and transmission. The results are presented in Columns II, IV, and VII–IX of Table I. The computed  $P^{\text{refl}}$  and  $P^{\text{trans}}$  values (Table I, Rows 8 and 9) were both converged to an absolute accuracy of around  $10^{-4}$  (last digit uncertain). For the Eckart A system (Column II), all parameters were taken directly from Ref. 4, except for the fixed (non-adaptive) Runge-Kutta time step size,  $\Delta$ , which was reconverged. For all other applications, a full reconvergence of all parameters was performed, as discussed above. For some systems, a direct comparison can be made between computed and exact (Rows 10 and 11)  $P^{\text{refl}}$  and  $P^{\text{trans}}$  values. For the Eckart systems, the exact results are known analytically.<sup>47</sup> For the uphill ramp system, “exact” values were obtained from a much more accurate numerical calculation, converged to at least eight significant digits.

In comparison with the corresponding calculations in Ref. 4, the converged parameter values are for the most part very similar, as expected. The glaring exception, of course, is the time step size,  $\Delta$ , whose values are found here to be *much* larger than in Ref. 4, owing to the use of fourth-order time integrators. More significant, however, is the fact that the present  $\Delta$  values are substantially larger than those of Ref. 3, which *also* employed non-adaptive fourth-order Runge-Kutta integration. For Eckart A for instance (Column II), the respective  $\Delta$  values (in atomic units) are as follows: Ref. 4, 0.156; Ref. 3, 10.0; present work, 156. The latter value is indeed very large for the level of accuracy achieved, and can be attributed to the numerical improvements introduced in Ref. 4. Remarkably, an even larger  $\Delta$  could in principle have been used here, but the value given is already so large that  $\Delta = t_{\text{shift}}$ . Thus, over a single time step, each grid point moves to a neighboring site—resulting in an effectively “fixed” grid that obviates both spatial differentiation<sup>3,4</sup> and interpolation. With regard to CPU effort, the Eckart A calculation performed here required 4.5 ms on a 2.60 GHz Pentium CPU, as compared with 1.7 s for Ref. 4. This reduction in CPU time is not as large as the 1000 $\times$  factor predicted by the increase in  $\Delta$ , owing to the fact that each Runge-Kutta iteration requires additional computation, but is nevertheless very substantial; the present calculation is also orders of magnitude faster than the corresponding Ref. 3 calculation.

In addition to the above investigation, we also examined the present method’s ability to provide extremely

accurate results. This was done in two distinct ways. First, a very deep tunneling study of the Eckart B system was performed, as presented in Table I, Columns V and VI. In effect, such a study evaluates absolute accuracy rather than precision—e.g. Column VI, for which the transmission probability is around  $10^{-9}$ , but is computed to only three significant digits. The method clearly works well in this context—although the greater the absolute accuracy level, the less the improvement relative to Ref. 4. For the  $E = 0.1V_0$  case, for instance,  $\Delta$  increases by only a factor of 25 $\times$ , which is less than  $t_{\text{shift}}$ , but only by a factor of two (Table I, Row 6). Second, in order to evaluate *precision* rather than absolute accuracy, we also performed an extremely accurate calculation of the  $E = V_0$  Eckart A system, for which both  $P^{\text{refl}}$  and  $P^{\text{trans}}$  were computed to *eleven* significant digits (Table I, Column III). As compared with Column II, the time step is reduced to an extent that is quantitatively consistent with a fourth-order integration method. The corresponding increase in grid size is difficult to predict quantitatively, but interestingly, is found to be such that the  $(t_{\text{shift}}/\Delta)$  ratio is again not far from one. Even for this extremely challenging application, the total CPU time required is only 36 seconds.

Despite the substantial breadth of the test suite applications considered, in all cases, the  $(t_{\text{shift}}/\Delta)$  ratios are on the order of one (Table I, Row 6)—a situation that bears further scrutiny. Accordingly, we conducted an additional calculation of the Eckart A system using *adaptive* (Cash-Karp) fifth-order Runge-Kutta integration<sup>48</sup>—the idea being that an adaptive method should automatically find the most appropriate time step sizes to use. In fact, using parameters similar to Column II, and specifying a target accuracy of  $5 \times 10^{-5}$ , we found the resultant  $\Delta$  values to be almost always equal to  $t_{\text{shift}}$ , except for the first few time steps, which had much smaller  $\Delta$  values. The resultant computed transmission and reflection probability errors (relative to exact analytical values) conform to the target accuracy level. One might conclude from the above that the corresponding *non*-adaptive calculation using fixed  $\Delta = t_{\text{shift}}$  would yield similar results. In fact, the latter calculation results in a near identical  $P^{\text{trans}}$  value, but a  $P^{\text{refl}}$  with an error of  $1.0 \times 10^{-3}$ . Thus, the initially small time steps appear to play a vital role, and also argue cogently in favor of adaptive time integration schemes.

## B. Multisurface Applications

We also performed numerical calculations for a variety of benchmark multisurface applications for  $f = 2$ , as described below.

- **Pure coupling:** asymptotically symmetric, with  $V_{ii}(x) = 0$  and Gaussian coupling.
- **Tully model 1:** crossed ramp potentials,  $V_{ii}(x)$ , with Gaussian coupling.

TABLE I: Parameters used for bipolar CPWM scattering calculations for single-surface test suite applications. All units are atomic units, except Row 12, the required CPU time in seconds on a 2.60 GHz Pentium CPU. Last digit of computed reflection and transmission probabilities (Rows 8 and 9) is uncertain.

Quantity and symbol	Single-surface test suite applications							
	Eckart A, $E = V_0$		Eckart B, $E =$			Uphill ramp	Barrier ramp	Double barrier
	low acc.	high acc.	$V_0$	$0.4 V_0$	$0.1 V_0$			
energy, $E$	0.001823	0.001823	0.011	0.0044	0.0011	0.0023	.0023	0.0014
grid size, $N$	20	800	25	61	110	19	15	20
left edge, $x_L$	-2.0	-4.0	-2.6	-3.5	-3.5	-1.5	-1.5	-2.2
right edge, $x_R$	2.0	4.0	2.1	4.0	3.5	2.2	2.0	2.2
time step, $\Delta$	156	2.47	19.7	14.9	30.62	107	125	196
# steps, $t_{\text{shift}}/\Delta$	1	3	3	4	2	2	2	1
max time, $t_{\text{max}}$	3899	11867	2893	43978	428621	5792	7000	39143
computed $P^{\text{reff}}$	.28348	.283...3842	.45967			.02391	.45455	.7958
computed $P^{\text{trans}}$	.71665	.716...6154	.537	1.560(-5)	9.923(-10)	.97595	.54562	.2053
exact $P^{\text{reff}}$	0.283358063869		.459605			.023901		
exact $P^{\text{trans}}$	0.716641936131		.540395	1.559(-5)	9.920(-10)	.976099		
CPU time (s)	0.0045	36	0.035	1.57	15	0.010	0.008	0.055

- **Tully model 2:** double avoided crossing, with  $V_{22}(x)$  a potential well.

These systems exhibit a very broad range of attributes, especially with respect to energy scale.

### 1. Pure coupling system

The two-surface pure coupling system is defined via

$$\begin{aligned} V_{11}(x) &= V_{22}(x) = 0 \\ V_{12}(x) &= V_0^{12} \exp[-\alpha(x - x_0)^2], \end{aligned} \quad (15)$$

with the parameter choices  $V_0^{12} = 150 \text{ cm}^{-1}$ ,  $x_0 = 0$ , and  $\alpha = 1 \text{ a.u.}$  This system represents an extreme case, in that there are no interaction potentials  $V_{i,i}$  to induce direct ( $+$   $\leftrightarrow$   $-$ ) transitions. Instead, any reflection must arise indirectly, from a successive pair of intersurface transitions. As is clear from Eq. (15), the pure coupling system above is asymptotically symmetric, implying that we can use uniform trajectories (which are also classical trajectories) and Eq. (9).

The energy  $E = 100 \text{ cm}^{-1} = (2/3)V_0^{12}$  is chosen to result in substantial probabilities for both scattered and unscattered wave components. Numerical calculations were performed using the algorithm of Sec. II C, with adaptive Cash-Karp integration as discussed in Sec. III A. All reflection and transmission probabilities were converged to an accuracy of  $10^{-5}$  or better, using the following parameter values:  $N = 61$ ;  $x_{L/R} = \mp 3 \text{ a.u.}$ ;  $t_{\text{max}} = 50000 \text{ a.u.}$ ; Runge Kutta tolerance level  $\epsilon = 10^{-6}$ .

The four resultant converged component densities,  $\rho_{1\pm}(x)$  and  $\rho_{2\pm}(x)$ , are plotted in Fig. 1 as a function of  $x$ . All four curves are smooth and interference-free, as desired, and satisfy the appropriate boundary conditions of Eq. (13). From Eq. (14), the various reflection and transmission probabilities are found to be as follows:  $P_1^{\text{reff}} = 0.17886$ ;  $P_2^{\text{reff}} = 0.22382$ ;  $P_1^{\text{trans}} = 0.12194$ ;

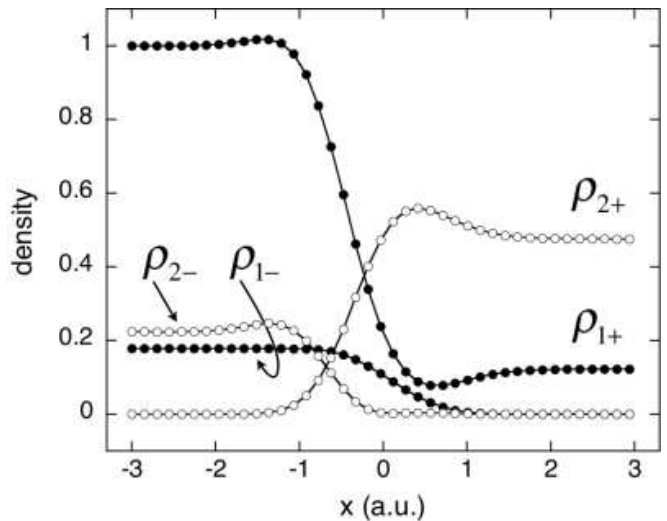


FIG. 1: Component wave densities as a function of position, for the two-surface pure coupling system (Sec. III B 1). Circles indicate trajectory grid points at the final time, for both diabatic states, 1 (filled circles) and 2 (open circles).

$P_2^{\text{trans}} = 0.47537$ . In Fig. 2, the two transmitted wave component densities,  $\rho_{1+}(x)$  and  $\rho_{2+}(x)$ , are summed together to form  $\rho_+(x)$ , and compared with the corresponding sum for the reflected components. As per the discussion at the end of Sec. II B, the two summed curves are indeed found to be identical—apart from a constant shift, represented by the dot-dashed line.

### 2. Tully Model 1

The Tully models were introduced in the early 1990's by John Tully and coworkers,<sup>32</sup> to serve as benchmark numerical applications for investigating various processes

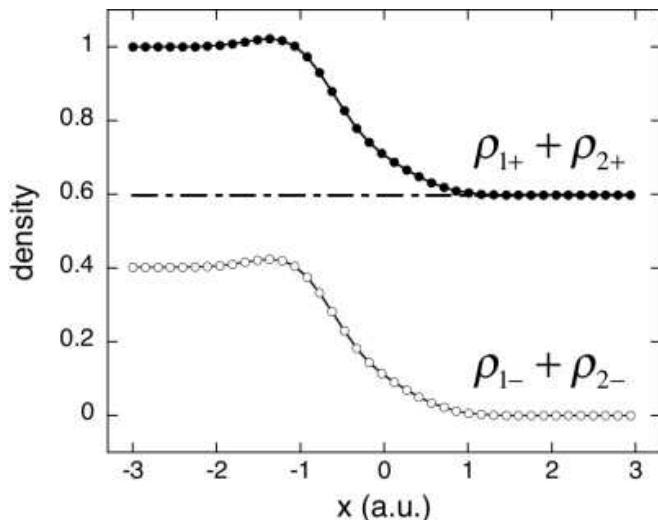


FIG. 2: Total transmitted (filled circles) and reflected (open circles) component wave densities (summed over all diabatic states) as a function of position, for the two-surface pure coupling system (Sec. III B 1). Circles indicate trajectory grid points at the final time,  $t = t_{\max}$ . Dot-dashed line indicates difference between the two curves—found to be a constant, equal to the total transmission probability.

involving electronic transitions.

The first Tully model is a simple avoided crossing system that consists of two diabatic ramp potentials—one an uphill ramp, and the other a downhill ramp—which cross each other symmetrically. For consistency and convenience, we have replaced Tully’s original piece-wise-exponential ramps with an analogous tanh functional form. The modified Tully Model 1 potentials are therefore as follows:

$$\begin{aligned} V_{11}(x) &= \left( \frac{V_R - V_L}{2} \right) \tanh[\beta(x - x_0)] \\ V_{22}(x) &= \left( \frac{V_L - V_R}{2} \right) \tanh[\beta(x - x_0)] \\ V_{12}(x) &= V_0^{12} \exp[-\alpha(x - x_0)^2], \end{aligned} \quad (16)$$

with parameters  $V_R = -V_L = 0.01$  hartree,  $x_0 = 0$ ,  $\beta = 1.2$  a.u.,  $V_0^{12} = 0.005$  hartree, and  $\alpha = 1$  a.u.

The diagonal potentials,  $V_{ii}(x)$ , are no longer symmetric, necessitating the use of Eq. (7) rather than Eq. (9). Due to the monotonicity of these potential curves, we take  $V_i^{\text{eff}}(x) = V_{ii}(x)$ , which results in standard classical trajectories for the bipolar CPWM dynamics. Note that there are now potential couplings that can induce direct transitions between any pair of  $\Psi_{1\pm}$  and  $\Psi_{2\pm}$  components. However, the energy value chosen,  $E = 0.11$  hartree ( $\approx 24142 \text{ cm}^{-1}$ ), is so much larger than the potential energy range as to ensure that there is negligible reflection. On the other hand, a substantial amount of intersurface coupling is obtained (Fig. 3).

Numerical calculations were performed as in Sec. III B 1, using the following parameter values:

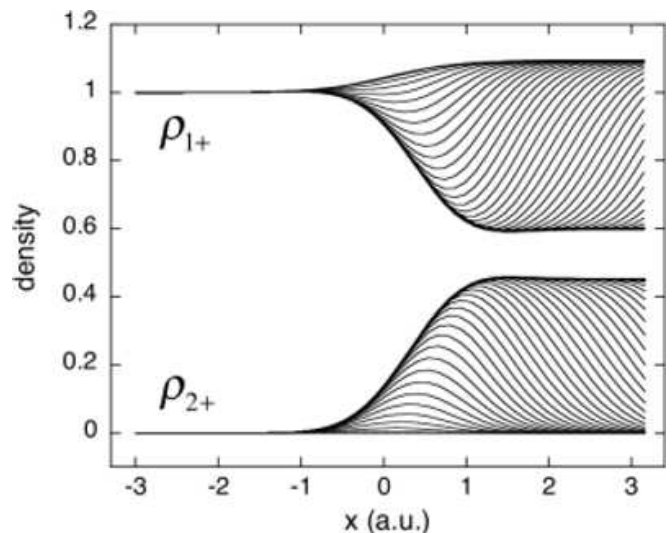


FIG. 3: Component transmitted wave densities as a function of position, and for a variety of times,  $t$ , for the two-surface Tully Model 1 system (Sec. III B 2). The upper family of curves represent  $\rho_{1+}(x)$  at different times, whereas the lower family of curves represent  $\rho_{2+}(x)$ . The highest  $\rho_{1+}$  curve is the  $t = 0$  initial value (i.e. the WKB approximation), whereas the lowest  $\rho_{2+}(x) = 0$  curve represents zero initial probability on diabatic state 2. Over time, probability is transferred from diabatic state 1 to 2 as indicated, via intersurface coupling.

$N = 50$ ;  $x_{L/R} = \mp 3$  a.u.;  $t_{\max} = 1000$  a.u.;  $\epsilon = 10^{-6}$ . An “animation plot” of the resultant time-dependent transmitted wave densities,  $\rho_{1+}(x, t)$  and  $\rho_{2+}(x, t)$ , is presented in Fig. 3. Each “contour line” is actually a snapshot of a given component density at a particular time,  $t$ . For  $\rho_{1+}$ , the uppermost curve is  $\rho_{1+}(x)$  at the initial  $t = 0$ , whereas the lowermost  $\rho_{1+}$  curve represents the  $t \rightarrow \infty$  limit. The opposite relation holds for the  $\rho_{2+}$  curves. From the figure, it is clear that the time evolution is smooth and well-behaved, and converges to the large-time limit quickly. The final curves represent essentially 100% transmission (the reflected wave densities are negligibly small, as expected), split roughly equally between the two curves as  $P_1^{\text{trans}} = 0.55016$  and  $P_2^{\text{trans}} = 0.44983$ .

In addition to the  $E = 0.11$  hartree case above, bipolar CPWM calculations were repeated and reconverged for a wide range of other energy values, to an accuracy of  $10^{-4}$  or better. Computed transmission probabilities for  $P_2^{\text{trans}}$  are presented in Fig. 4, and found to be in excellent agreement with the quantum results of Herman.<sup>49</sup>

### 3. Tully Model 2

The second Tully model is a more complex, double avoided crossing system. The two diabatic curves consist of a symmetric well, and a constant energy curve which cuts across the well, giving rise to avoided crossings at the two intersections. These in turn give rise to quantum



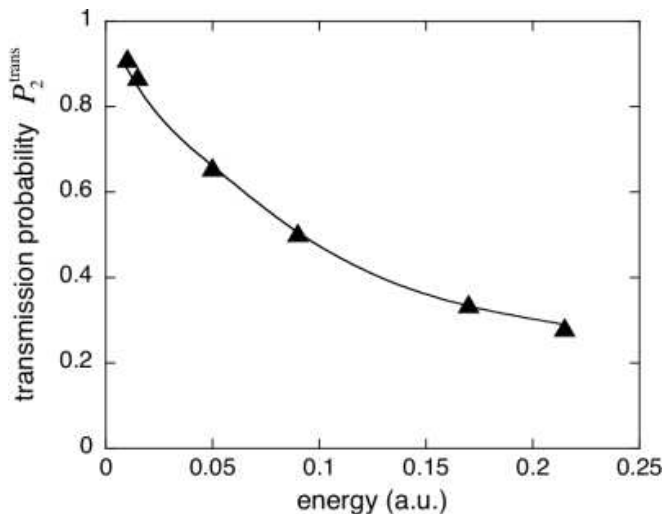


FIG. 4: Computed transmission probabilities  $P_2^{\text{trans}}$  vs energy  $E$ , for the two-surface Tully Model 1 system (Sec. III B 2). Filled triangles indicate present results, as obtained using the classical trajectory CPWM bipolar decomposition; solid curve indicates quantum results of Herman.<sup>49</sup>

interference effects.<sup>32,50</sup> The potentials are

$$\begin{aligned} V_{11}(x) &= 0 \\ V_{22}(x) &= -V_0 \exp[-\beta(x - x_0)^2] + E_0 \\ V_{12}(x) &= V_0^{12} \exp[-\alpha(x - x_0)^2], \end{aligned} \quad (17)$$

with parameters  $V_0 = 0.10$  hartree,  $x_0 = 0$ ,  $\beta = 0.28$  a.u.,  $E_0 = 0.05$  hartree,  $V_0^{12} = 0.015$  hartree, and  $\alpha = 0.06$  a.u.

The diagonal potentials are symmetric, and therefore amenable to uniform trajectories. However, the energies involved are so large and “classical-like” that it is better to use standard classical trajectories,  $V_i^{\text{eff}}(x) = V_{ii}(x)$ . Note that  $V_{22}$  describes a potential well, thus ensuring that there will be no turning points. The large energies also ensure that reflection is negligible, but again, there is substantial intersurface coupling. Depending on the energy, the following range of parameters were used to achieve a convergence of  $10^{-2}$  or better:  $N = 200\text{--}300$ ;  $x_{L/R} = \mp 8$  a.u.;  $t_{\text{max}} = 1000\text{--}2000$  a.u.;  $\epsilon = 10^{-4}$ .

Quantum interference associated with the two different surface pathways manifests as two distinct types of “Stückelberg oscillations,”<sup>32,50,51,52</sup> both associated with the Stückelberg phase difference,<sup>52,53</sup>

$$\Delta\Phi_{12} \approx \left(\frac{1}{\hbar}\right) \int \left[ \sqrt{2m(E - V_{11})} - \sqrt{2m(E - V_{22})} \right] dx'. \quad (18)$$

Evaluating Eq. (18) as a definite integral over the relevant range of  $x'$  yields oscillations in  $P_1^{\text{trans}}$  as a function of  $E$ . The computed transmission probabilities over a range of  $E$  values are presented in Fig. 5; these are indeed oscillatory, and also in good agreement with Ref. 49.

The second type of Stückelberg oscillation is obtained by integrating Eq. (18) to the indefinite limit,  $x$ , which

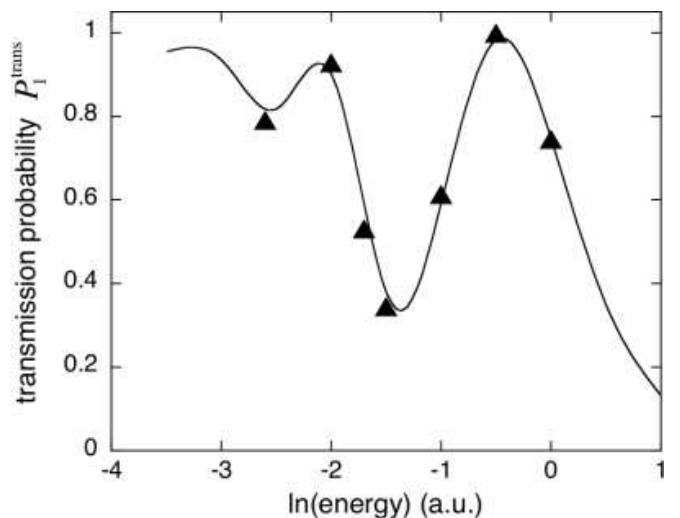


FIG. 5: Computed transmission probabilities  $P_1^{\text{trans}}$  vs logarithm of energy  $E$ , for the two-surface Tully Model 2 system (Sec. III B 3). Filled triangles indicate present results, as obtained using the classical trajectory CPWM bipolar decomposition; solid curve indicates quantum results of Herman.<sup>49</sup> Note the Stückelberg oscillations.

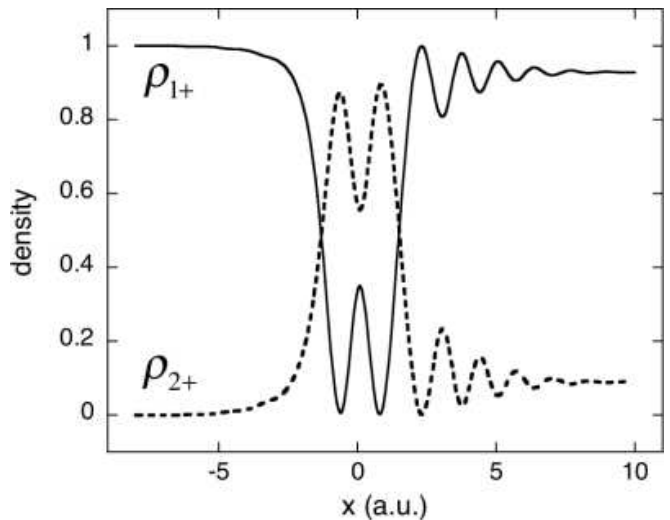


FIG. 6: Component transmitted wave densities,  $\rho_{1+}$  (solid) and  $\rho_{2+}$  (dashed), as a function of position, for the two-surface Tully Model 2 system (Sec. III B 3). The oscillatory transfer of probability is a type of Stückelberg phenomenon.

can give rise to oscillations in  $\rho_i(x) \approx \rho_{i+}(x)$ . Oscillations are indeed observed in the converged transmitted wave densities for the  $E = \exp(-2) \approx 0.13533$  hartree case considered, as presented in Fig. 6. The asymptotic oscillation wavelength as predicted by Eq. (18) is found to be 1.31 a.u., in good agreement with the figure.

#### IV. CONCLUSION

From a numerical perspective, the straight fourth-order Runge-Kutta bipolar CPWM algorithm, incorporating the numerical refinements of Ref. 4, is found in Sec. III A to satisfy the demands of numerical stability, robustness, efficiency, and minimal user intervention. In particular, this algorithm is remarkably efficient at both high and low levels of absolute accuracy, and also for very high precision calculations such as Table I Column III. We believe this algorithm to be the fastest available for computing stationary scattering states of single-surface 1D systems with predetermined boundary conditions, and advocate its use as a “black-box” method that can be applied to virtually any such application. That the algorithm also generalizes to *multisurface* 1D applications in straightforward fashion (Sec. II C), is also significant. We note that for systems such as Tully Model 2, exhibiting substantial intersurface but little (+ ↔ −) interference effects, the bipolar CPWM in its present incarnation necessarily undergoes a noticeable drop in efficiency, as the Stückelberg oscillations must manifest in the component field functions. However, Fig. 6 suggests that it may be possible to generalize the theory for arbitrary electronic representations (i.e. neither diabatic nor adiabatic) in such a way as to avoid interference oscillations altogether in such cases. In any event, well-documented stand-alone fortran codes for the one- and two-surface algorithms considered here are available from the authors on request.

Note that although little explicit connection with conventional “Bohmian mechanics” *per se* has been made in this work—i.e. of “polar” (amplitude-phase) decompositions of the wavefunction components, and quantum potentials—implicitly, it is precisely this connection that enables the algorithms used here to work so well, as discussed in detail in the previous publications, notably Refs. 3 and 4. Of course, it is possible to recast Eqs. (7) and (9) in polar form, yielding more explicitly “Bohm-like” results. Indeed, this is the usual convention in the prior semiclassical literature,<sup>8</sup> and we have also done this. However, this results in more complicated evolution equations that obscure aspects of the physics which we wish to emphasize in this work. Note that from a *numerical* perspective however, we use *both* polar and non-polar representations at different stages in the algorithm, transforming between them as described in Ref. 4 [Eq. (9)].

From a theoretical perspective, the multisurface generalization of the F approach with generalized classical trajectories (Sec. II B) presents some very intriguing aspects, with possible significance beyond the scope of the present paper. To begin with, the flux relations of Eqs. (10) through (12) provide a natural, but non-trivial, multi-surface-like interpretation to the flow of probability among all  $2f$  of the “components,”  $\Psi_{i\pm}$ . Even more compelling, however, is the form of the dynamical equations

of Eq. (9), which above all serves to highlight the essential sameness of the two types of transitions—intersurface and (+ ↔ −)—now treated together within a single unified framework. That off-diagonal diabatic potentials induce transitions from one surface to another has always been known; now we find that in similar fashion, *diagonal* potentials also induce transitions, between transmitted and reflected components of the wavefunction associated with a given diabatic state.

The above picture can lead one in a variety of interesting directions. Traditional TSH methods, for instance,<sup>31,32</sup> utilize off-diagonal coupling<sup>53</sup> as a means of inducing trajectory hops from one surface to another. The present work suggests that a similar TSH scheme could be applied to effect transitions from reflected to transmitted wavepackets (even for single-surface calculations), thereby naturally introducing interference and other effects that might otherwise be problematic in a traditional TSH context. Such a method would first require that a non-stationary, *wavepacket* generalization of the present work be developed; indeed, this will serve as the focus of the next publication in the series, with the subsequent paper addressing multidimensional applications. Note that both of these future papers will more directly emphasize the link with Bohmian mechanics—restoring the quantum potential, for example, which is required for wavepackets, but not essential for stationary state applications. As a bit of foreshadowing to motivate the present work, we comment that the multidimensional generalization still requires only *two* components per electronic state (regardless of system dimensionality), and can accommodate standard Jacobi-type coordinate representations with arbitrary curvilinear reaction paths.

Finally, we briefly mention two other possible areas for future development. First, the present theory is restricted to potentials that are asymptotically flat in *both* asymptotes,  $x \rightarrow \infty$  and  $x \rightarrow -\infty$ . It would be useful to generalize for potentials that are singular, or otherwise diverge in one asymptote or the other. Second, the intriguing result from Table I Row 6 that ( $t_{\text{shift}}/\Delta$ ) is always on the order of one suggests that simply *setting* this value to one would not adversely affect numerical efficiency too severely. Indeed, such a modification would lead to some decided numerical advantages, such as the use of fixed grids which would avoid the need for intrasurface (but not intersurface) interpolation. The resultant grid densities would be larger, however, and for this reason, such an approach might be substantially less efficient for high dimensionalities.

#### Acknowledgments

This work was supported by a grant from The Welch Foundation (D-1523). Jason McAfee is also acknowledged for his aid in converting this manuscript to an electronic format suitable for the arXiv preprint server.

- \* Electronic address: Bill.Poirier@ttu.edu  
† Electronic address: Gerard.Parlant@univ-montp2.fr
- <sup>1</sup> B. Poirier, *J. Chem. Phys.* **121**, 4501 (2004).
  - <sup>2</sup> C. Trahan and B. Poirier, *J. Chem. Phys.* **124**, 034115 (2006).
  - <sup>3</sup> C. Trahan and B. Poirier, *J. Chem. Phys.* **124**, 034116 (2006).
  - <sup>4</sup> B. Poirier, *J. Theo. Comput. Chem.* **6**, 99 (2007).
  - <sup>5</sup> D. Babyuk and R. E. Wyatt, *J. Chem. Phys.* **121**, 9230 (2004).
  - <sup>6</sup> R. E. Wyatt, *Quantum Dynamics with Trajectories: Introduction to Quantum Hydrodynamics* (Springer, New York, 2005).
  - <sup>7</sup> J. Heading, *An Introduction to Phase-integral Methods* (Methuen, London, 1962).
  - <sup>8</sup> N. Fröman and P. O. Fröman, *JWKB Approximation* (North-Holland, Amsterdam, 1965).
  - <sup>9</sup> M. V. Berry and K. V. Mount, *Rep. Prog. Phys.* **35**, 315 (1972).
  - <sup>10</sup> C. L. Lopreore and R. E. Wyatt, *Phys. Rev. Lett.* **82**, 5190 (1999).
  - <sup>11</sup> F. S. Mayor, A. Askar, and H. A. Rabitz, *J. Chem. Phys.* **111**, 2423 (1999).
  - <sup>12</sup> R. E. Wyatt, *Chem. Phys. Lett.* **313**, 189 (1999).
  - <sup>13</sup> D. V. Shalashilin and M. S. Child, *J. Chem. Phys.* **113**, 10028 (2000).
  - <sup>14</sup> R. E. Wyatt, C. L. Lopreore, and G. Parlant, *J. Chem. Phys.* **114**, 5113 (2001).
  - <sup>15</sup> R. E. Wyatt and E. R. Bittner, *J. Chem. Phys.* **113**, 8898 (2001).
  - <sup>16</sup> R. E. Wyatt and K. Na, *Phys. Rev. E* **65**, 016702 (2001).
  - <sup>17</sup> C. L. Lopreore and R. E. Wyatt, *J. Chem. Phys.* **116**, 1228 (2002).
  - <sup>18</sup> I. Burghardt and L. S. Cederbaum, *J. Chem. Phys.* **115**, 10312 (2001).
  - <sup>19</sup> E. R. Bittner, J. B. Maddox, and I. Burghardt, *Int. J. Quantum Chem.* **89**, 313 (2002).
  - <sup>20</sup> K. H. Hughes and R. E. Wyatt, *Phys. Chem. Chem. Phys.* **5**, 3905 (2003).
  - <sup>21</sup> D. Frenkel and B. Smit, *Understanding Molecular Simulations* (Academic, New York, 2002).
  - <sup>22</sup> E. Madelung, *Z. Phys.* **40**, 322 (1926).
  - <sup>23</sup> J. H. van Vleck, *Proc. Natl. Acad. Sci. U.S.A.* **14**, 178 (1928).
  - <sup>24</sup> D. Bohm, *Phys. Rev.* **85**, 166 (1952).
  - <sup>25</sup> D. Bohm, *Phys. Rev.* **85**, 180 (1952).
  - <sup>26</sup> T. Takabayasi, *Prog. Theor. Phys.* **11**, 341 (1954).
  - <sup>27</sup> P. R. Holland, *The Quantum Theory of Motion* (Cambridge University Press, Cambridge, 1993).
  - <sup>28</sup> C. J. Trahan and R. E. Wyatt, *J. Chem. Phys.* **118**, 4784 (2003).
  - <sup>29</sup> B. K. Kendrick, *J. Chem. Phys.* **119**, 5805 (2003).
  - <sup>30</sup> D. K. Pauler and B. K. Kendrick, *J. Chem. Phys.* **120**, 603 (2004).
  - <sup>31</sup> J. C. Tully and P. K. Preston, *J. Chem. Phys.* **55**, 562 (1971).
  - <sup>32</sup> J. C. Tully, *J. Chem. Phys.* **93**, 1061 (1990).
  - <sup>33</sup> V. A. Rassolov and S. Garashchuk, *Phys. Rev. A* **71**, 032511 (2005).
  - <sup>34</sup> S. Garashchuk, V. A. Rassolov, and G. C. Schatz, *J. Chem. Phys.* **123**, 174108 (2005).
  - <sup>35</sup> J. C. Burant and J. C. Tully, *J. Chem. Phys.* **112**, 6097 (2000).
  - <sup>36</sup> M. H. Alexander, G. Parlant, and T. H. Hemmer, *J. Chem. Phys.* **91**, 2388 (1989).
  - <sup>37</sup> M. H. Alexander, *J. Chem. Phys.* **95**, 8931 (1991).
  - <sup>38</sup> D. V. Shalashilin, A. V. Michtchenko, and F. Lara, *Chem. Phys. Lett.* **207**, 250 (1993).
  - <sup>39</sup> D. V. Shalashilin, *Chem. Phys. Lett.* **233**, 161 (1995).
  - <sup>40</sup> see for example, *Int. J. Quant. Chem.* **14**, (1978), special issue.
  - <sup>41</sup> W. P. Reinhardt, *Ann. Rev. Phys. Chem.* **33**, 223 (1982).
  - <sup>42</sup> V. Ryaboy, N. Moiseyev, V. A. Mandelshtam, and H. S. Taylor, *J. Chem. Phys.* **101**, 5677 (1994).
  - <sup>43</sup> T. Seideman and W. H. Miller, *J. Chem. Phys.* **96**, 4412 (1992).
  - <sup>44</sup> U. V. Riss and H.-D. Meyer, *J. Phys. B: At. Mol. Phys.* **26**, 4503 (1993).
  - <sup>45</sup> B. Poirier and T. Carrington, Jr., *J. Chem. Phys.* **118**, 17 (2003).
  - <sup>46</sup> J. G. Muga, J. P. Palao, B. Navarro, and I. L. Egusquiza, *Phys. Rep.* **395**, 357 (2004).
  - <sup>47</sup> Z. Ahmed, *Phys. Rev. A* **47**, 4761 (1993).
  - <sup>48</sup> W. H. Press *et al*, in *Numerical Recipes*, 1st ed. (Cambridge University Press, Cambridge, England, 1989).
  - <sup>49</sup> Y. Wu and M. F. Herman, *J. Chem. Phys.* **123**, 144106 (2005).
  - <sup>50</sup> C.-C. Wan and J. Schofield, *J. Chem. Phys.* **113**, 7047 (2000).
  - <sup>51</sup> E. E. Nikitin, *Theory of Elementary Atomic and Molecular Processes in Gases* (Clarendon, Oxford, 1974).
  - <sup>52</sup> *Atomic, Molecular, and Optical Physics Handbook*, edited by G. W. F. Drake (AIP Press, New York, 1996).
  - <sup>53</sup> Strictly speaking adiabatic potentials should be used, but this distinction is immaterial for the present discussion.